

Article

Multi-Criteria Optimization of Automatic Electro-Spark Deposition TiCrNiVSi_{0.1} Multi-Principal Element Alloy Coating on TC4 Alloy

Yong Lian ^{1,2,*} , Menghui Cui ^{1,2}, Aihua Han ^{1,2}, Zhao Liu ^{1,2} and Jin Zhang ^{1,2,*}

¹ Institute for Advanced Materials and Technology, University of Science and Technology Beijing, Beijing 100083, China

² Beijing Key Laboratory for Corrosion Erosion and Surface Technology, Beijing 100083, China

* Correspondence: liany09@126.com (Y.L.); zhangjin@ustb.edu.cn (J.Z.); Tel.: +86-10-82377393 (Y.L.)

Abstract: In this work, TiCrNiVSi_{0.1} coatings were prepared on TC4 alloy by CNC-controlled automatic electro-spark deposition (ESD). The TOPSIS-based Taguchi method was applied for multi-criteria optimization of ESD coating quality. Frequency (f), capacitance (c), and electrode moving speed (v) were considered process parameters for optimizing the coating quality criteria, which included coating thickness, coating coverage, and porosity in the coating. The optimized parametric setting of the ESD process (f = 700 Hz, c = 270 μF, v = 150 mm/min) was obtained. MPEA coatings with a thickness of about 70 μm, a coverage rate almost reaching 100%, and porosity as low as about 1% were prepared. The wear- and burn-resistance functions of the TiCrNiVSi_{0.1} ESD coatings were investigated. The wear rates of the coating at room temperature and 400 °C are one-sixth and one-fourth of the TC4 alloy, respectively. A TiCrNiVSi_{0.1} alloy coating was deposited and significantly improved the burn resistance of the TC4 alloy.

Keywords: electro-spark deposition; multi-criteria optimization; multi-principal element alloy; coating



Citation: Lian, Y.; Cui, M.; Han, A.; Liu, Z.; Zhang, J. Multi-Criteria Optimization of Automatic Electro-Spark Deposition TiCrNiVSi_{0.1} Multi-Principal Element Alloy Coating on TC4 Alloy. *Coatings* **2023**, *13*, 214. <https://doi.org/10.3390/coatings13010214>

Academic Editors: Frederic Sanchette and Giorgos Skordaris

Received: 6 December 2022

Revised: 27 December 2022

Accepted: 13 January 2023

Published: 16 January 2023



Copyright: © 2023 by the authors. Licensee MDPI, Basel, Switzerland. This article is an open access article distributed under the terms and conditions of the Creative Commons Attribution (CC BY) license (<https://creativecommons.org/licenses/by/4.0/>).

1. Introduction

Due to the high strength-to-weight ratio, high specific modulus, and excellent corrosion resistance, titanium alloys are widely used in aerospace, automotive, military, and sports [1]. However, titanium alloys burn easily due to the low thermal coefficient and high combustion heat, commonly referred to as “titanium fire” [2,3]. Titanium fire can be ignited by high-speed friction and strong impact, especially under the conditions of high pressure and high temperature, and aero engines are a typical scenario. Moreover, they can self-sustain combustion even in air, which can hardly be controlled and may lead to catastrophic accidents [4,5]. The increasing application of titanium alloys runs the risk of ignition and combustion, which promotes the application and development of burn-resistant coatings on titanium alloys.

High-entropy alloys, also known as multicomponent or multi-principal element alloys (MPEA), developed in the last few decades overturn the previous alloy design strategies of adding relatively small amounts of secondary elements to a primary element, which have remained unchanged over millennia [6]. Different from traditional alloys, which have a single principal element, MPEAs are mostly composed of five or more elements, where the content of each element varies from 5 to 35 at. %. The mixing of elements in this composition produces severe lattice torsion, sluggish diffusion, the cocktail effect, and high mixing entropy, which gives rise to outstanding mechanical strength, high thermal stability, superior wear resistance, and excellent corrosion resistance [7]. With the properties mentioned above, MPEAs have been considered as attractive coating materials for providing protection to surfaces exposed to harsh environments. By appropriate selection of the

alloying elements and adjusting the compositions, these alloys can enhance the surface properties of substrates to achieve desired performance, such as superior oxidation, wear, and corrosion resistance. In general, most MPEA coatings reported are based on Ni, Co, and Fe [8–10]. Nevertheless, the investigation of MPEA coating-based Ti has scarcely been reported. In this paper, TiCrNiVSi_{0.1} MPEA coatings were designed to fabricate coatings for improving the surface properties of TC4 alloy. Ti-based MPEA coatings were prepared because they usually possess a similar coefficient of thermal expansion as the titanium alloy substrate [11]. Ni was added as it possesses flame-retardant properties [12]. At the same time, Cr and Si were added to ensure good corrosion and oxidation resistance [13] and further improve the flame-retardant capacity.

Based on the advancement of MPEAs, various technologies have been applied concerning the application of MPEA films and coatings. Most of these methods are based on vapor deposition [14,15], laser cladding [13,16,17], and thermal spraying [18,19]. However, due to the high total heat input of a laser or arc, it is crucial to control the residual stress of the deposited coatings and deformation of the substrates [8,20,21]. The equipment for vapor deposition is relatively complicated, and the coating deposited is relatively thin with low efficiency [22]. Therefore, research attention has been focused on developing excellent coatings on titanium alloys by other possible methods [23,24]. Electro-spark deposition (ESD), a pulsed-arc microwelding process that uses short-duration, high-current electrical pulses to build up metallurgical coatings, can enhance the various surface performances of workpieces without changing the shape and inherent properties of the matrix materials [25]. With a small amount of material deposited per pulse, the cooling rates can reach 10⁶ °C/s [26], which facilitates the formation of a high-entropy solution microstructure in MPEA. This makes the ESD process quite suitable for the deposition of MPEA coatings on titanium alloys. Recently, ESD has been widely used in many areas, although most of them are manipulated manually. The ESD coating quality varies with each individual, as it is not easy to control the deposition parameters by hand [27–29]. However, reports on ESD coatings prepared by automated apparatus are extremely rare. Automation of the ESD process provides significant advantages, which allow the easy control of several important parameters that are otherwise difficult to control by hand.

In this paper, the multi-objective optimization of the ESD process of TiCrNiVSi_{0.1} MPEA coatings on TC4 alloys was performed. The experiments were performed on an automatic ESD system. Movements of MPEA electrodes have been controlled through computed numerically controlled (CNC) programming. The technique for order of preference by similarity ideal solution (TOPSIS) based on the Taguchi method was applied for multi-criteria optimization in ESD coating quality. The optimal process parameters were obtained under these conditions. Then, the wear- and burn-resistance functions of the TiCrNiVSi_{0.1} coatings were investigated.

2. Materials and Methods

Commercial TC4 titanium alloy (Ti-6Al-4V) specimens with dimensions of 100 mm × 50 mm × 10 mm were used as the substrate materials. The specimens were ground with SiC abrasive paper up to 1200# to remove the contaminants and oxide films. TiCrNiVSi_{0.1} alloys (18.89 wt.% Ti, 26.64 wt.% Cr, 25.13 wt.% V, and 1.39 wt.% Si) were arc-melted and solidified in a water-cooled copper crucible in the argon atmosphere. Cylindrical electrodes with a diameter of 3 mm were cut from a TiCrNiVSi_{0.1} alloy-cast ingot by electro-discharge machining. ESD apparatus was built based on the ESD-300 type ESD deposition system. The apparatus used is shown in Figure 1. Throughout our work, the ESD torch was attached to a three-axis XYZ table, which can be controlled by CNC. The rotating electrode (anode) was fixed to the Z-axis, and TC4 specimens (cathode) were fixed on the X-Y platform. The whole ESD apparatus, besides the power supply, was placed in a closed chamber to ensure the ESD process with well-shielded inert gas. In the deposition process, the deposition electrode was kept in continuous contact with the substrate during

the deposition process. The electrode moving strategy is shown in Figure 1. A consistent gap of 0.5 mm was selected based on the analysis of the pre-research experiment.

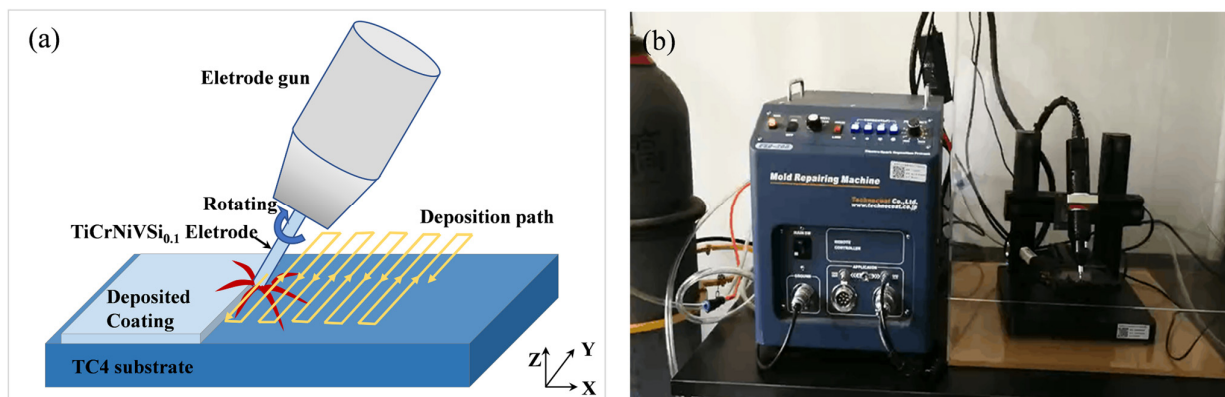


Figure 1. Illustration for CNC automatic electro-spark deposition (a) and photograph of an automatic electro-spark deposition experimental device (b).

Frequency (f), capacitance (c), and electrode moving speed (v) were considered as process parameters for optimizing the coating quality criteria, which include coating thickness, coating coverage, and porosity in coating based on Taguchi L16 orthogonal experimental design, as shown in Table 1.

Table 1. Design of Taguchi L16 orthogonal experimental parameters.

Factors	Unit	Level 1	Level 2	Level 3	Level 4
Frequency	Hz	150	260	360	700
Capacitance	μF	180	210	240	270
Electrode moving speed	mm/min	100	150	200	250

The sample was cut perpendicular to the deposition direction, then ground to 2000# on SiC sandpapers, and polished with a 2 μm alumina suspension. Finally, the specimens were corroded in Keller reagent for 5 s. The cross-sectional micromorphology of the ESD coatings was observed using a scanning electron microscope (SEM, Zeiss GeminiSEM 300, Carl Zeiss Microscopy Ltd., Cambridge, UK) equipped with an energy dispersive spectrometer (EDS, Oxford X-MAX 50, Oxford Instruments Inc., Oxford, UK). The phase composition of the TC4 substrate before and after ESD deposition was determined using an X-ray diffractometer (XRD, Bruker D8 ADVANCE, BRUKER AXS Inc., Karlsruhe, Germany) with a scanning rate of 4°/min in the diffraction angle range of 20°~90°. The average thickness of the coating was determined by measuring ten different areas of the sample cross-sections, and the average value was taken. The coating porosity was evaluated by measuring the area proportion of pores in the whole coating cross-section with Image J software. The coatings' coverage was measured based on ten random metallographic observations of the ESD sample cross-section as follows:

$$Cov = \left(\frac{L_1}{L} \right) \times 100\% \quad (1)$$

where Cov is the coating coverage; L is the total length of the observed cross-section, in μm ; L_1 is the total ESD coating coverage length, in μm , as shown in Figure 2.

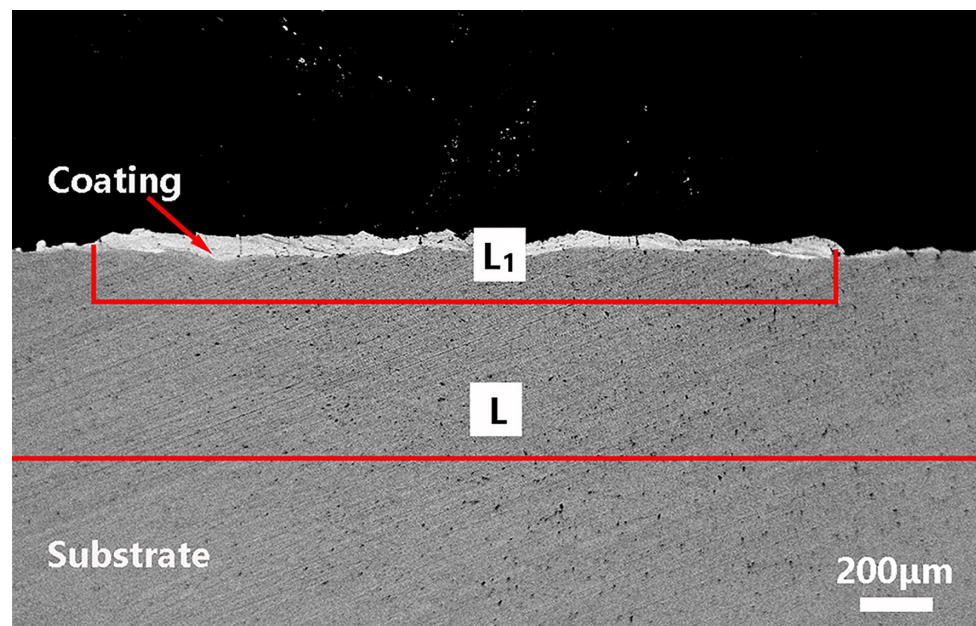


Figure 2. Schematic diagram of coverage calculation.

The technique for order of preference by similarity ideal solution (TOPSIS) was used to optimize the coating quality criteria, which include coating thickness, coating coverage, and porosity in coating. Several samples were prepared under the optimized ESD process. Hardness measurements were made using the Vickers hardness test method under a load of 200 g and a loading time of 15 s. The test was repeated five times to ensure accuracy.

Wear- and burn-resistance functions of the TiCrNiVSi_{0.1} coatings were investigated. Wear resistance tests of TC4 and ESD coatings were carried out on a ball-on-disc MG-2000 wear test apparatus equipped with a heater at room temperature (RT) and 400 °C. TC4 and ESD coating samples were selected as discs, and Si₃N₄ balls with a diameter of 3 mm were used as the grinding balls. Experiments were carried out at 25 °C and 600 °C with a load of 50 N and a wear distance of 5 mm. The rotation speed was set at 400 r/min and the total time of tests for each group was 5 min. The wear rate was calculated through the volume loss divided by sliding distance, where the volume loss was calculated based on the depth and width of the wear track measured by a Keyence V_k-200 laser confocal microscope, as per the method in Ref. [30]. Morphology and composition of the worn surface were examined by a JEOL-6000-PLUS desktop scanning electron microscope equipped with energy-dispersive X-ray spectroscopy (EDS, Excel Technologies, Inc., Enfield, CT, USA). The burn-resistance test of TC4 alloy and TiCrNiVSi_{0.1}-coated alloy was evaluated using the laser spot melting test. A fiber laser (1.5 kW) with a wavelength of 1080 nm was used to irradiate the specimen with a 300 W laser beam with a spot diameter of 1 mm. The laser exposure time for each specimen was 5 s. The 3D surface morphology of the TC4 and TiCrNiVSi_{0.1}-coated samples after the laser spot melting test was measured by a Keyence V_k-200 laser confocal microscope (Keyence Corporation, Osaka, Japan).

3. Results and Discussion

3.1. Multi-Criteria Optimization of Automatic ESD Process

In the present work, experiments were designed using the Taguchi orthogonal array, which involves three input parameters, each with four levels. The order of the run and experimental design matrix is shown in Table 2. It can be found that there are different optimal responses for the three quality criteria. So, the technique for order of preference by similarity to ideal solution (TOPSIS) was applied for multi-criteria optimization in ESD coating quality.

Table 2. Orthogonal test design and response calculation results.

No.	Input Parameters			Output Responses			Normalized Matrix Values (r_{ij})		
	f (Hz)	c (μ F)	v (mm/min)	T (μ m)	Cov (%)	I (%)	T	Cov	I
1	150	180	100	55.82	95.00	1.355	0.63	0.91	0.65
2	150	210	150	44.78	83.90	1.569	0.31	0.66	0.44
3	150	240	200	33.64	54.99	1.278	0.00	0.00	0.72
4	150	270	250	41.57	83.36	1.026	0.22	0.65	0.97
5	260	180	150	36.84	90.97	0.996	0.09	0.82	1.00
6	260	210	100	40.61	89.16	1.158	0.20	0.78	0.84
7	260	240	250	43.57	90.28	1.212	0.28	0.81	0.79
8	260	270	200	49.30	91.01	1.453	0.44	0.82	0.55
9	360	180	200	48.97	98.54	1.363	0.43	0.99	0.64
10	360	210	250	43.66	85.65	1.058	0.28	0.70	0.94
11	360	240	100	48.07	81.89	1.416	0.41	0.61	0.59
12	360	270	150	58.98	88.40	1.432	0.72	0.76	0.57
13	700	180	250	54.49	96.56	1.387	0.59	0.95	0.62
14	700	210	200	52.85	79.04	1.788	0.54	0.55	0.23
15	700	240	150	63.02	96.58	1.235	0.83	0.95	0.77
16	700	270	100	69.02	98.78	2.021	1.00	1.00	0.00

The ESD experimental matrix and the measured responses are shown in Table 2. In the process of multi-response optimization for different experimental results, there were different dimensions and units for different results, so various experimental results cannot be directly compared. Therefore, the average thickness, coverage, and porosity of different dimensions were normalized.

The TOPSIS process is carried out as follows:

Step 1: Normalization of the decision matrix; the normalized output responses are shown in Table 2. The normalized value r_{ij} is calculated as follows:

$$r_{ij} = \frac{R_{max} - R_{ij}}{R_{max} - R_{min}}, \quad i = 1, 2, \dots, 16; \quad j = 1, 2, 3 \quad (2)$$

here i = no. of experimental runs, j = no. of output responses, R_{ij} = value of i th experimental run associated with the j th output response, R_{max} is the maximum response value and R_{min} is the minimum response value of the j th output response.

Step 2: Calculation of weighted normalized decision matrix. In the weighted normalized decision matrix v_{ij} was obtained as Equation (3).

$$v_{ij} = w_j \cdot r_{ij}, \quad i = 1, 2, \dots, 16; \quad j = 1, 2, 3 \quad (3)$$

here r_{ij} is the normalized value, w_j is the weighted value. in this work, the entropy weight method [31] was used to weigh the normalized experimental data, and the weighted values are listed in Table 3.

Table 3. Entropy method to calculate the weight results.

Response Value	Information Entropy (e)	Information Utility Value (d)	Weight Factor (w)
Thickness	0.9313	0.0687	51.47%
Coverage	0.9729	0.0271	20.27%
Porosity	0.9623	0.0377	28.26%

Step 3: Determine the positive and negative ideal solutions S^+ and S^- , respectively.

$$S^+ = \{(\max v_{ij}) | j \in J_1, (\min v_{ij}) | j \in J_2\}, \quad i = 1, 2, \dots, 16; \quad j = 1, 2, 3 \quad (4)$$

$$S^- = \{(\min v_{ij}) | j \in J_1, (\max v_{ij}) | j \in J_2\}, \quad i = 1, 2, \dots, 16; \quad j = 1, 2, 3 \quad (5)$$

here J_1 is associated with the benefit criteria, and J_2 is associated with the cost criteria. In this work, $S^+ = [0.5147, 0.2027, 0.2826]$, $S^- = [0, 0, 0]$.

Step 4: Calculate the Euclidean distance for each row from the ideal worst and the ideal best values.

$$S_i^+ = \sqrt{\sum_{j=1}^3 (v_{ij} - S_j^+)^2}, i = 1, 2, \dots, 16; j = 1, 2, 3 \tag{6}$$

$$S_i^- = \sqrt{\sum_{j=1}^3 (v_{ij} - S_j^-)^2}, i = 1, 2, \dots, 16; j = 1, 2, 3 \tag{7}$$

here S_i^+ is the best distance calculated of an i th row, S_j^+ is the ideal best for that column. Similarly, we can find S_i^- , i.e., worst distance calculated on an i th row.

Step 5: Calculate the closeness coefficient for all alternatives and rank them according to the closeness coefficient C_i^* , i.e., the higher the coefficient, the better the rank.

$$C_i^* = \frac{S_i^-}{S_i^+ + S_i^-}, i = 1, 2, \dots, 16 \tag{8}$$

The weighted normalized values for thickness, coverage, and porosity are listed in Table 4. The positive and negative ideal solutions S_i^+ and S_i^- and the closeness of each experimental result to the optimal ideal solution C_i^* are also listed in Table 4. It can be found that the C_i^* value of experiment No. 15 ranks the highest. This indicated that the process parameters of experiment No. 15 ($f = 700$ Hz, $c = 240$ μ F, $v = 150$ mm/min) were the closest to the optimal setting.

Table 4. Calculated v_{i1} , S_i^+ , S_i^- , and their closeness coefficient to the ideal solution.

No.	v_{i1}	v_{i2}	v_{i3}	S_i^+	S_i^-	C_i^*	Rank
1	0.3243	0.1845	0.1837	0.217	0.415	0.657	4
2	0.1596	0.1338	0.1243	0.392	0.244	0.384	15
3	0	0	0.2035	0.559	0.205	0.268	16
4	0.1132	0.1318	0.2741	0.406	0.325	0.445	12
5	0.0463	0.1662	0.2826	0.470	0.331	0.414	14
6	0.1029	0.1581	0.2374	0.418	0.303	0.420	13
7	0.1441	0.1642	0.2233	0.377	0.312	0.453	11
8	0.2265	0.1662	0.1554	0.315	0.323	0.506	7
9	0.2213	0.2007	0.1809	0.309	0.351	0.532	6
10	0.1441	0.1419	0.2656	0.374	0.334	0.472	9
11	0.2110	0.1236	0.1667	0.335	0.296	0.469	10
12	0.3706	0.1541	0.1611	0.195	0.431	0.689	2
13	0.3037	0.1926	0.1752	0.237	0.399	0.627	5
14	0.2779	0.1115	0.0650	0.334	0.308	0.480	8
15	0.4272	0.1926	0.2176	0.110	0.516	0.825	1
16	0.5147	0.2027	0	0.283	0.553	0.662	3

The optimal solution can be obtained using the range method. The mean values of the closeness of the ideal response values corresponding to the process parameters were shown in Table 5. It can be found that frequency was the most remarkable effect factor on the thickness and porosity of the coating, while capacitance had the most significant influence on the coverage of the coating. Among the process parameters, as shown in Figure 3, the frequency has the largest range (Max.–Min.), so it can be concluded that the frequency was the most remarkable effect factor on the quality of the coating, while electrode moving speed has the least effect. So far, a multi-criteria optimization results can be obtained; that is, the optimized parametric setting of the ESD process was $f = 700$ Hz, $c = 270$ μ F, $v = 150$ mm/min.

Table 5. Response table for mean closeness coefficient C_i^* .

Process Parameters	Average Closeness Coefficient				Max.–Min.
	Level 1	Level 2	Level 3	Level 4	
Frequency	0.4385	0.4482	0.5405	0.6485	0.2100
Capacitance	0.5575	0.4390	0.5037	0.5755	0.1365
Electrode moving speed	0.5520	0.5780	0.4465	0.4993	0.1315

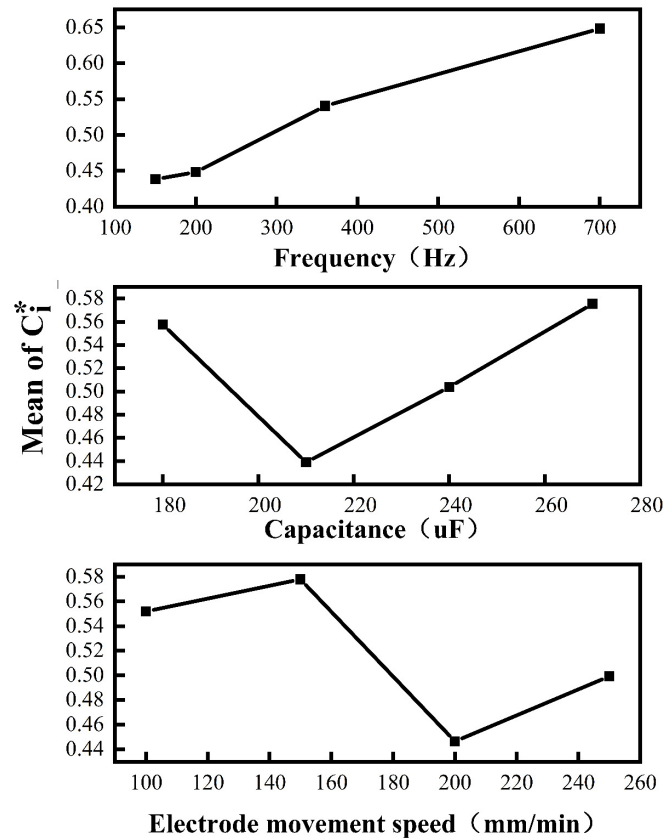
**Figure 3.** Mean graph of closeness coefficient C_i^* .

Figure 4a shows the microscopic appearance of the TiCrNiVSi_{0.1} ESD coating deposited on TC4 using the final optimized process parameters of $f = 700$ Hz, $c = 270$ μ F, $v = 150$ mm/min. TiCrNiVSi_{0.1} coatings with an average thickness of about 70 μ m were prepared under the optimum ESD parameters. The coverage rate of the MPEA coatings almost reached 100%, and the porosity was as low as about 1%. The XRD patterns of T- TiCrNiVSi_{0.1} ESD coating and TC4 alloy substrate are presented in Figure 4b. The patterns of ESD coating, diffraction lines belonging to a body-centered cubic (BCC) solid solution beside the hexagonal close-packed (HCP) Laves phase, verify the formation of MPEA coating. The TOPSIS-based Taguchi method can be an effective way to multi-criteria optimize the quality of multi-principal element alloy coatings deposited by CNC-controlled automatic ESD.

3.2. Wear Resistance of TiCrNiVSi_{0.1} ESD Coating

Figure 5a shows the microhardness comparison between the TC4 substrate and the TiCrNiVSi_{0.1} alloy coating. TiCrNiVSi_{0.1} alloy coatings deposited on TC4 improved the hardness of the surface. Figure 5b shows the wear rates of the TC4 titanium alloy substrate and the TiCrNiVSi_{0.1} alloy coating at room temperature and 400 °C. It can be seen from Figure 5b that the wear rate of the coating at room temperature and 400 °C is one-sixth and one-fourth of the TC4 alloy, respectively. Compared with the TC4 alloy substrate, the

existence of the $\text{TiCrNiVSi}_{0.1}$ alloy coating can effectively improve the wear resistance of the titanium alloy surface.

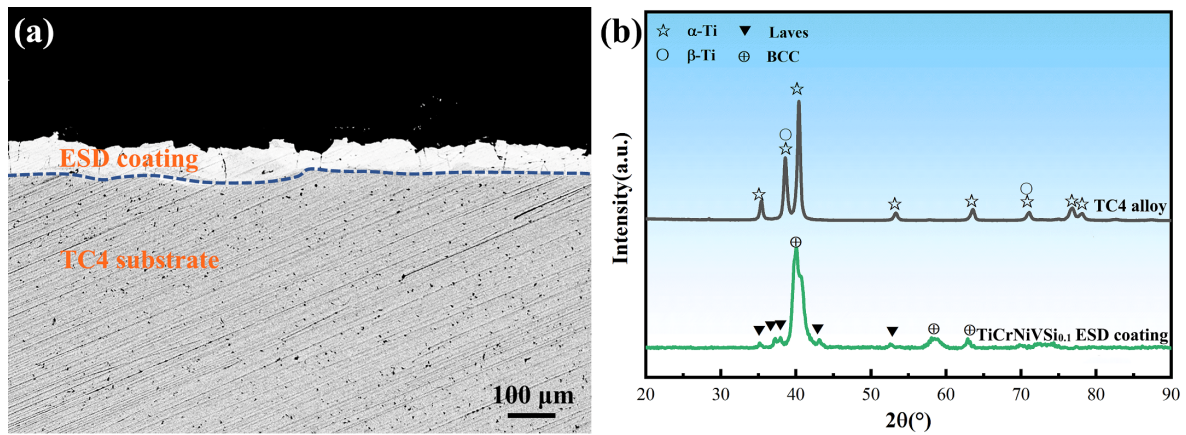


Figure 4. Cross-section morphology (a) and XRD pattern (b) of $\text{TiCrNiVSi}_{0.1}$ ESD coating deposited on a TC4 alloy substrate under the optimized process parameters.

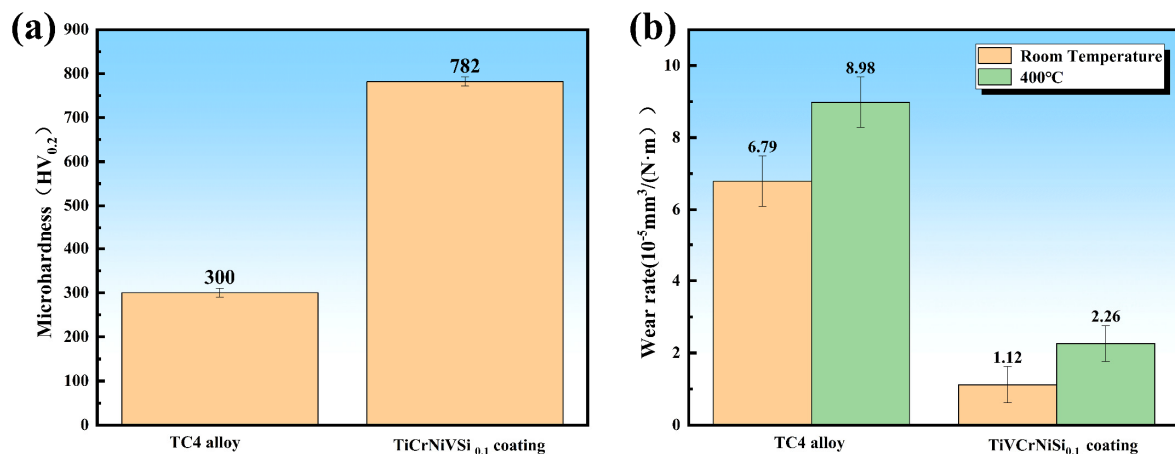


Figure 5. (a) Microhardness of the TC4 alloy and $\text{TiCrNiVSi}_{0.1}$ coating, and (b) wear rate of the $\text{TiCrNiVSi}_{0.1}$ coating and TC4 alloy at room temperature and 400 °C.

Figure 6 shows the wear morphologies of a TC4 alloy substrate and a $\text{TiCrNiVSi}_{0.1}$ alloy coating at room temperature and 400 °C. Wear grooves and wear debris can be found on both TC4 alloy and $\text{TiCrNiVSi}_{0.1}$ coating specimens after a wear test at room temperature, as shown in Figure 6a,b. The abrasive particles of the $\text{TiCrNiVSi}_{0.1}$ alloy coating are finer and more uniform. In the process of friction and wear, many uniformly dispersed particles were extruded and cut into finer powdery debris embedded in the substrate, which showed typical abrasive wear behavior [32]. The decrease in wear rate of TC4 alloys deposited with $\text{TiCrNiVSi}_{0.1}$ coatings can be explained based on the following two factors. First, the deposited $\text{TiCrNiVSi}_{0.1}$ alloy coating was rich in Ti and Cr. Ti and Cr elements [33] in the alloy coating form oxides, and the oxide film existing on the surface can improve the wear resistance. Second, the $\text{TiCrNiVSi}_{0.1}$ alloy coating is composed of the BCC and Laves phases. Like other hard phase [34–36], the hard Laves phase particles undergo surface brittle failure, forming wear debris between the ball and the alloy. Three-body wear formed between the Laves hard particles, Si_3N_4 grinding balls, and the alloy surface, which resulted in a slight three-body abrasive wear.

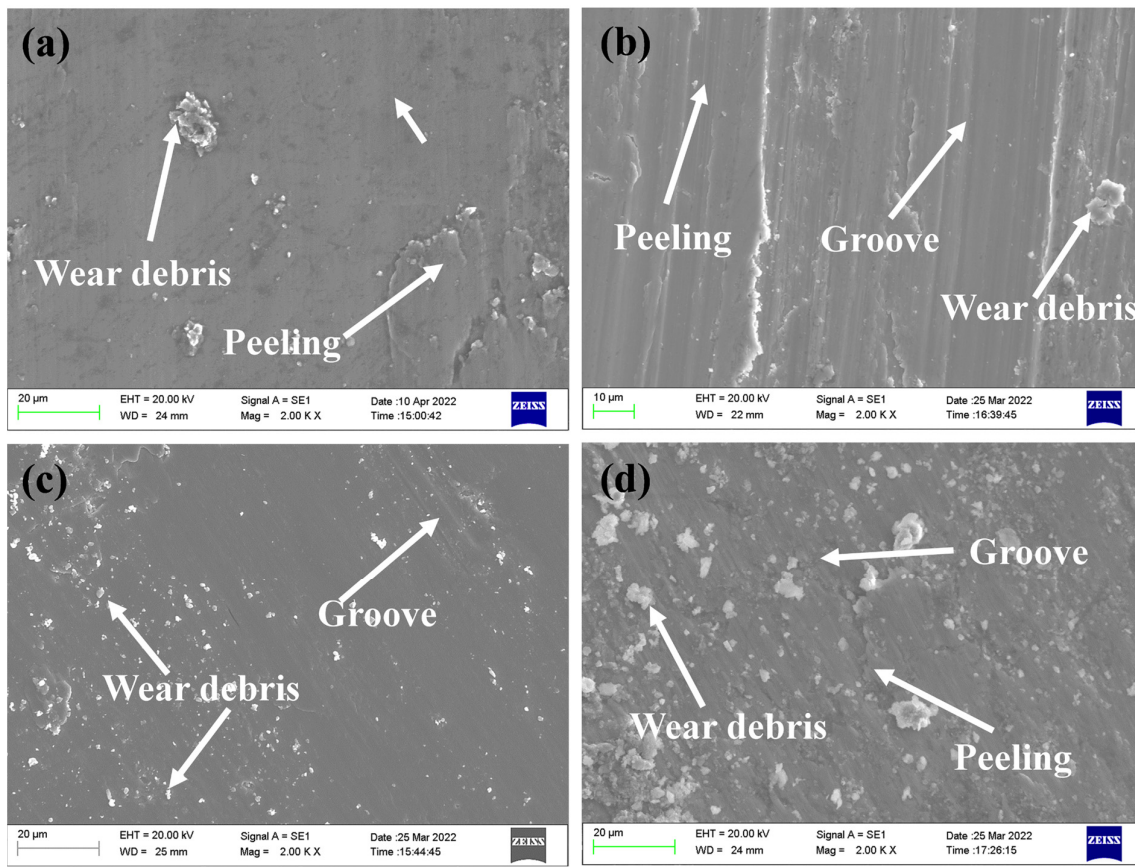


Figure 6. Wear morphologies of the coating at (a) room temperature and (b) 400 °C, and wear morphologies of the TC4 alloy at (c) room temperature and (d) 400 °C.

Combined with the EDS results as shown in Table 6, it can be found that slight oxidative wear occurs on the coating surface during the wear test at 400 °C. The decrease in wear rates of TC4 alloy and ESD coating may be due to the formation of oxide film during the wear test at 400 °C. The formation of oxide film may own to the dual action of temperature and heat generated during friction [37]. Studies have shown that oxides can provide a protective effect even when they are not incomplete [38,39]. During wear, the oxide layer on the surface of the alloy underwent a cycle of cracking, spalling, and recompositing. In this process, the oxide layer acts as an intermediate protector.

Table 6. EDS results of the typical region of worn surface of TC4 alloy and TiCrNiVSi_{0.1} ESD coating samples after wear tests at room temperature and 400 °C.

Sample	T (°C)	Elemental Content (at. %) of Worn Surface							
		Ti	V	Cr	Ni	Mn	Si	O	Al
TiCrNiVSi _{0.1} ESD coating	RT	66.4	8.1	6.4	9.8	-	2.0	-	7.3
	400	62.1	8.5	5.3	5.2	-	2.0	12.1	5.8
TC4 alloy	RT	85.3	4.3	-	-	-	-	-	10.4
	400	73.1	2.9	-	-	-	-	14.5	9.5

3.3. Burn Resistance of TiCrNiVSi_{0.1} ESD Coating

Figure 7 shows the morphologies of the TC4 alloy and TiCrNiVSi_{0.1} ESD coating after laser ablation. After the laser spot ablation, the surface of the sample is severely oxidized and burned. A portion of the molten alloy is evaporated or splashed, leaving an ablation pit on the laser-molten surface, as shown in Figure 7. The ablation pit size parameters of TC4 alloy and TiCrNiVSi_{0.1} alloy coatings after laser ablation are shown in Table 7. For the TC4 alloy, the laser melting zone is approximately 1400 µm in diameter, including the

surrounding combustion products and a central circular blind hole (Figure 7a), with a depth of approximately 1200 μm . The laser fusion zone for the TiCrNiVSi_{0.1} coating sample is relatively flat and daisy-shaped, with the central blind hole disappearing (Figure 7b). For TiCrNiVSi_{0.1} coating samples, the ablation pores are only 366 μm in depth and 986 μm in diameter, indicating that TiCrNiVSi_{0.1} alloy coating deposited on TC4 substrate significantly improves the burn resistance of TC4 alloy.

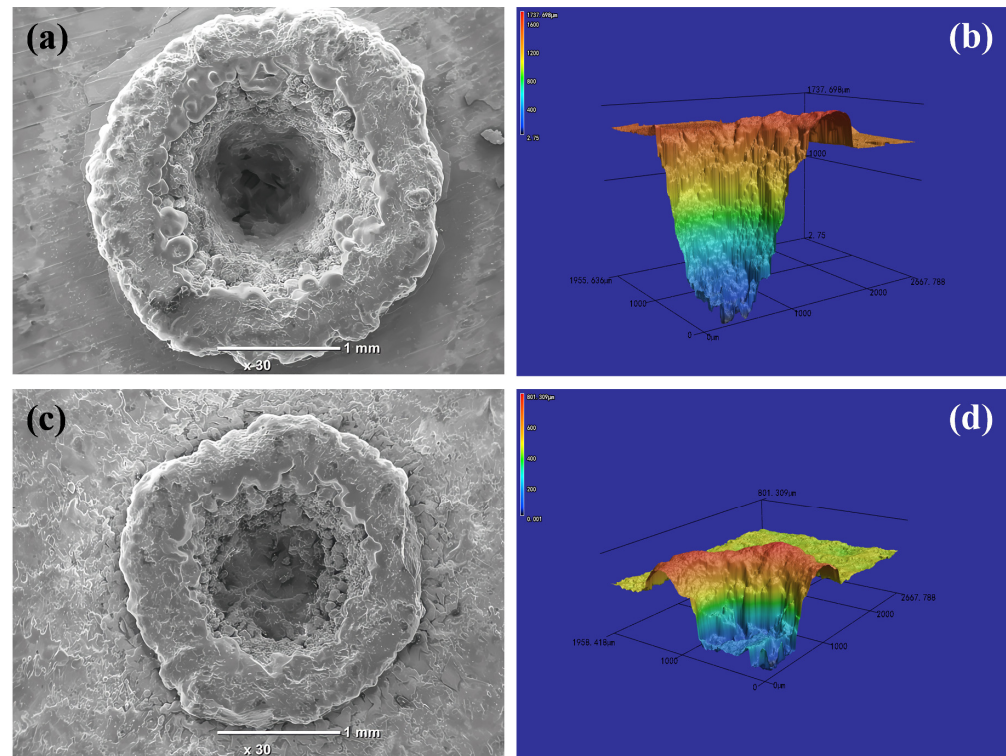


Figure 7. Morphologies of TC4 alloy (a,b) and TiCrNiVSi_{0.1} alloy coating (c,d) after laser ablation.

Table 7. Ablation pit size parameters of TC4 alloy and TiCrNiVSi_{0.1} alloy coatings after laser ablation.

Pit Size Parameter (um)	TC4	TiCrNiVSi _{0.1}
Diameter	986.15	366.49
Depth	1378.71	1216.61

The improvement in the burn resistance of TC4 alloy can be explained on the basis of two factors. First, the elements composed in the TiCrNiVSi_{0.1} alloy effectively reduce the combustion heat of the system. It can be seen from the Ellingham diagram [40] that the heat of the oxidation reaction of Ni, Cr, V, and Si elements is much lower than that of titanium. Second, the thermal conductivity of the TiCrNiVSi_{0.1} alloy and TC4 alloy tests at 800 °C is 29.1 W/(M·K) and 21.0 W/(M·K), respectively. This shows that the thermal conductivity of the TiCrNiVSi_{0.1} alloy coating is higher than that of the TC4 alloy. The ESD coating has better heat dissipation ability than TC4 alloy, reducing the accumulation of heat and making the heat distribution more uniform, thereby reducing the probability of ignition.

4. Conclusions

The automatic ESD deposition coating process was optimized by Taguchi and TOPSIS methods, and the performance of a multi-principal element alloy coating was tested. The main findings can be summarized as follows:

- (1) The experimental operation was conducted using the Taguchi L16 orthogonal array, and the TOPSIS method was used to solve the multi-objective optimization problem.

TiCrNiVSi_{0.1} coatings with an average thickness of about 70 μm, the coverage rate almost reached 100%, and porosity as low as 1% were prepared under the optimal ESD process.

- (2) The wear rates of the ESD coating at room temperature and 400 °C are one-sixth and one-fourth of the TC4 alloy, respectively. The wear type of ESD coating changes from single abrasive wear at room temperature to a mixture of abrasive and oxidative wear at 400 °C.
- (3) TiCrNiVSi_{0.1} coating can effectively prevent the combustion spread caused by the injection of energy; the depth and width of the molten pool after the combustion of ESD coatings are significantly smaller than that of a titanium alloy substrate.

Author Contributions: Conceptualization, Y.L.; investigation, M.C., A.H. and Z.L.; writing—original draft preparation, M.C. and Y.L.; writing—review and editing, Y.L.; supervision, Y.L. and J.Z.; funding acquisition, Y.L. All authors have read and agreed to the published version of the manuscript.

Funding: This research was funded by the National Natural Science Foundation of China (Grant No.51901016) and the Fundamental Research Funds for the Central Universities (FRF-TP-18-031A2, FRF-GF-18-024B).

Institutional Review Board Statement: Not applicable.

Informed Consent Statement: Not applicable.

Data Availability Statement: The data that support the findings of this study are available within the article.

Conflicts of Interest: The authors declare no conflict of interest.

References

1. Shao, L.; Xie, G.L.; Liu, X.; Wu, Y.; Tan, Q.; Xie, L.; Xin, S.W.; Hao, F.; Yu, J.B.; Xue, W.L.; et al. Combustion behavior and mechanism of Ti-25V-15Cr compared to Ti-6Al-4V alloy. *Corros. Sci.* **2022**, *194*, 109957. [[CrossRef](#)]
2. Li, B.; Ding, R.D.; Shen, Y.F.; Hu, Y.Z.; Guo, Y. Preparation of Ti–Cr and Ti–Cu flame-retardant coatings on Ti-6Al-4V using a high-energy mechanical alloying method: A preliminary research. *Mater. Des.* **2012**, *35*, 25–36. [[CrossRef](#)]
3. Yeh, J.W.; Chen, S.K.; Lin, S.J.; Gan, J.Y.; Chin, T.S.; Shun, T.T.; Tsau, C.H.; Chang, S.Y. Nanostructured high-entropy alloys with multiple principal elements: Novel alloy design concepts and outcomes. *Adv. Eng. Mater.* **2004**, *6*, 299–303. [[CrossRef](#)]
4. Estrada-Guel, I.; Rodríguez-González, C.A.; Hernández-Paz, J.; Jimenez, O.; Santos-Beltran, A.; Martínez-Sánchez, R.; Romero-Romero, M.; Gómez-Esparza, C.D. Phase composition and its effect on the mechanical performance of an AlCoCrFeNiTi high-entropy alloy. *Mater. Lett.* **2022**, *316*, 132035. [[CrossRef](#)]
5. Wu, P.F.; Gan, K.F.; Yan, D.S.; Fu, Z.H.; Li, Z.M. A non-equiatom FeNiCoCr high-entropy alloy with excellent anti-corrosion performance and strength-ductility synergy. *Corros. Sci.* **2021**, *183*, 109341. [[CrossRef](#)]
6. Geng, Y.S.; Chen, J.; Tan, H.; Cheng, J.; Zhu, S.Y.; Yang, J. Tribological performances of CoCrFeNiAl high entropy alloy matrix solid-lubricating composites over a wide temperature range. *Tribol. Int.* **2021**, *157*, 106912. [[CrossRef](#)]
7. Yan, Y.G.; McGarrity, K.A.; Delia, D.J.; Fekety, C.; Wang, K. The oxidation-resistance mechanism of WTaNbTiAl refractory high entropy alloy. *Corros. Sci.* **2022**, *204*, 110377. [[CrossRef](#)]
8. Ma, M.Y.; Xiong, W.J.; Lian, Y.; Han, D.; Zhao, C.; Zhang, J. Modeling and optimization for laser cladding via multi-objective quantum-behaved particle swarm optimization algorithm. *Surf. Coat. Technol.* **2020**, *381*, 125129. [[CrossRef](#)]
9. Li, Y.T.; Wang, C.T.; Ma, D.L.; Zeng, X.K.; Liu, M.; Jiang, X.; Leng, Y.X. Nano dual-phase CuNiTiNbCr high entropy alloy films produced by high-power pulsed magnetron sputtering. *Surf. Coat. Technol.* **2021**, *420*, 127325. [[CrossRef](#)]
10. Swain, B.; Priyadarshini, M.; Mohapatra, S.S.; Gupta, R.K.; Behera, A. Parametric optimization of atmospheric plasma spray coating using fuzzy TOPSIS hybrid technique. *J. Alloys Compd.* **2021**, *867*, 159074. [[CrossRef](#)]
11. Shafyei, H.; Salehi, M.; Bahrami, A. Fabrication, microstructural characterization and mechanical properties evaluation of Ti/TiB/TiB₂ composite coatings deposited on Ti6Al4V alloy by electro-spark deposition method. *Ceram. Int.* **2020**, *46*, 15276–15284. [[CrossRef](#)]
12. Gao, Z.N.; Wang, L.L.; Wang, Y.N.; Lyu, F.Y.; Zhan, X.H. Crack defects and formation mechanism of FeCoCrNi high entropy alloy coating on TC4 titanium alloy prepared by laser cladding. *J. Alloys Compd.* **2022**, *903*, 163905. [[CrossRef](#)]
13. Ma, M.Y.; Han, A.H.; Zhang, Z.J.; Lian, Y.; Zhao, C.; Zhang, J. The role of Si on microstructure and high-temperature oxidation of CoCr₂FeNb_{0.5}Ni high-entropy alloy coating. *Corros. Sci.* **2021**, *185*, 109417. [[CrossRef](#)]
14. Fan, X.; Zheng, S.J.; Ren, S.M.; Pu, J.B.; Chang, K.K. Effects of phase transition on tribological properties of amorphous VAlTiCrSi high-entropy alloy film by magnetron sputtering. *Mater. Charact.* **2022**, *191*, 112115. [[CrossRef](#)]

15. Lin, C.H.; Duh, J.G. Corrosion behavior of (Ti–Al–Cr–Si–V)_xNy coatings on mild steels derived from RF magnetron sputtering. *Surf. Coat. Technol.* **2008**, *203*, 558–561. [[CrossRef](#)]
16. Sun, Z.L.; Zhang, M.Y.; Wang, G.Q.; Yang, X.F. Wear and Corrosion Resistance Analysis of FeCoNiTiAl_x High-Entropy Alloy Coatings Prepared by Laser Cladding. *Coatings* **2021**, *11*, 155. [[CrossRef](#)]
17. Zhang, H.X.; Dai, J.J.; Sun, C.X.; Li, S.Y. Microstructure and wear resistance of TiAlNiSiV high-entropy laser cladding coating on Ti-6Al-4V. *J. Mater. Proc. Technol.* **2020**, *282*, 116671. [[CrossRef](#)]
18. Wang, L.M.; Chen, C.C.; Yeh, J.W.; Ke, S.T. The microstructure and strengthening mechanism of thermal spray coating Ni_xCo_{0.6}Fe_{0.2}Cr_ySi_zAlTi_{0.2} high-entropy alloys. *Mater. Chem. Phys.* **2011**, *126*, 880–885. [[CrossRef](#)]
19. Wang, W.R.; Qi, W.; Xie, L.; Yang, X.; Li, J.T.; Zhang, Y. Microstructure and Corrosion Behavior of (CoCrFeNi)₉₅Nb₅ High-Entropy Alloy Coating Fabricated by Plasma Spraying. *Materials* **2019**, *12*, 694. [[CrossRef](#)]
20. Sharma, A. High Entropy Alloy Coatings and Technology. *Coatings* **2021**, *11*, 372. [[CrossRef](#)]
21. Baltatu, M.S.; Vizureanu, P.; Sandu, A.V.; Munteanu, C.; Istrate, B. Microstructural Analysis and Tribological Behavior of Ti-Based Alloys with a Ceramic Layer Using the Thermal Spray Method. *Coatings* **2020**, *10*, 1216. [[CrossRef](#)]
22. Hong, X.; Feng, K.; Tan, Y.F.; Wang, X.L.; Tan, H. Effects of process parameters on microstructure and wear resistance of TiN coatings deposited on TC11 titanium alloy by electrospark deposition. *Trans. Nonferr. Met. Soc. China* **2017**, *27*, 1767–1776. [[CrossRef](#)]
23. Baltatu, M.S.; Sandu, A.V.; Nabialek, M.; Vizureanu, P.; Ciobanu, G. Biomimetic Deposition of Hydroxyapatite Layer on Titanium Alloys. *Micromachines* **2021**, *12*, 1447. [[CrossRef](#)]
24. Liu, Y.; Wang, D.P.; Deng, C.Y.; Huo, L.X.; Wang, L.J.; Fang, R. Novel method to fabricate Ti–Al intermetallic compound coatings on Ti–6Al–4V alloy by combined ultrasonic impact treatment and electrospark deposition. *J. Alloys Compd.* **2015**, *628*, 208–212. [[CrossRef](#)]
25. Wang, X.R.; Wang, Z.Q.; Lin, T.S.; He, P. Mass transfer trends of AlCoCrFeNi high-entropy alloy coatings on TC11 substrate via electro-spark computer numerical control deposition. *J. Mater. Process. Technol.* **2017**, *241*, 93–102. [[CrossRef](#)]
26. Myslyvchenko, O.M.; Gaponova, O.P.; Tarelnyk, V.B.; Krapivka, M.O. The structure formation and hardness of high-entropy alloy coatings obtained by electrospark deposition. *Powder Metall. Met. Ceram.* **2020**, *59*, 201–208. [[CrossRef](#)]
27. Wang, D.; Gao, J.H.; Zhang, R.; Deng, S.J.; Jiang, S.Y.; Cheng, D.H.; Liu, P.; Xiong, Z.Y.; Wang, W.Q. Effect of TaC particles on the microstructure and oxidation behavior of NiCoCrAlYTa coating prepared by electrospark deposition on single crystal superalloy. *Surf. Coat. Technol.* **2021**, *408*, 126851. [[CrossRef](#)]
28. Barile, C.; Casavola, C.; Pappalettera, G.; Renna, G. Advancements in Electrospark Deposition (ESD) Technique: A Short Review. *Coatings* **2022**, *12*, 1536. [[CrossRef](#)]
29. Renna, G.; Leo, P.; Casalino, G.; Cerri, E. Repairing 2024 Aluminum Alloy via Electrospark Deposition Process: A Feasibility Study. *Adv. Mater. Sci. Eng.* **2018**, *2018*, 8563054. [[CrossRef](#)]
30. Zhu, Z.X.; Liu, X.B.; Liu, Y.F.; Zhang, S.Y.; Meng, Y.; Zhou, H.B.; Zhang, S.H. Effects of Cu/Si on the microstructure and tribological properties of FeCoCrNi high entropy alloy coating by laser cladding. *Wear* **2023**, *512–513*, 204533. [[CrossRef](#)]
31. Yang, T.; Chou, P. Solving a multiresponse simulation-optimization problem with discrete variables using a multiple-attribute decision-making method. *Math. Comput. Simul.* **2005**, *68*, 9–21. [[CrossRef](#)]
32. Low, D.; Sumii, T.; Swain, M. Thermal expansion coefficient of titanium casting. *J. Oral Rehabil.* **2001**, *28*, 239–242. [[CrossRef](#)]
33. Bi, Y.B.; Xu, Y.; Zhang, Y.; Xue, R.L.; Bao, Y. Single-pass laser welding of TC4 Ti alloy to 304 SS with V interlayer and V/Cu bilayer. *Mater. Lett.* **2021**, *285*, 129072. [[CrossRef](#)]
34. Deng, C.; Wang, C.; Chai, L.J.; Wang, T.; Luo, J. Mechanical and chemical properties of CoCrFeNiMo_{0.2} high entropy alloy coating fabricated on Ti6Al4V by laser cladding. *Intermetallics* **2022**, *144*, 107504. [[CrossRef](#)]
35. Zhang, T.G.; Zhuang, H.F.; Zhang, Q.; Yao, B.; Yang, F. Influence of Y₂O₃ on the microstructure and tribological properties of Ti-based wear-resistant laser-clad layers on TC4 alloy. *Ceram. Int.* **2020**, *46*, 13711–13723. [[CrossRef](#)]
36. Cai, F.; Zhang, J.M.; Wang, J.M.; Zheng, J.; Wang, Q.M.; Zhang, S.H. Improved adhesion and erosion wear performance of CrSiN/Cr multi-layer coatings on Ti alloy by inserting ductile Cr layers. *Tribol. Int.* **2021**, *153*, 106657. [[CrossRef](#)]
37. Ma, Q.S.; Li, Y.J.; Wang, J.; Liu, K. Microstructure evolution and growth control of ceramic particles in wide-band laser clad Ni60/WC composite coatings. *Mater. Des.* **2016**, *92*, 897–905. [[CrossRef](#)]
38. Wang, W.Q.; Zhang, S.Q.; Xiao, S.; Sato, Y.S.; Wang, D.; Liu, Y.; Liu, D.L.; Hu, Q. Microstructure and properties of multilayer WC-40Co coating on Ti-6Al-4V by electron beam cladding. *Mater. Charact.* **2022**, *183*, 111585. [[CrossRef](#)]
39. Sun, Q.C.; Hu, T.C.; Fan, H.Z.; Zhang, Y.S.; Hu, L.T. Thermal oxidation behavior and tribological properties of textured TC4 surface: Influence of thermal oxidation temperature and time. *Tribol. Int.* **2016**, *94*, 479–489. [[CrossRef](#)]
40. Gaskell, D.R.; Laughlin, D.E. *Introduction to the Thermodynamics of Materials*; CRC Press: Boca Raton, FL, USA, 2017. [[CrossRef](#)]

Disclaimer/Publisher’s Note: The statements, opinions and data contained in all publications are solely those of the individual author(s) and contributor(s) and not of MDPI and/or the editor(s). MDPI and/or the editor(s) disclaim responsibility for any injury to people or property resulting from any ideas, methods, instructions or products referred to in the content.